

FULL ARTICLE

Hyperspectral multimodal CARS microscopy in the fingerprint region

Adrian F. Pegoraro^{**},^{1,2}, Aaron D. Slepov^{**},^{2,3}, Andrew Ridsdale¹, Douglas J. Moffatt¹, and Albert Stolow^{*},^{1,2}

¹ Department of Physics, Queen's University, Kingston, Ontario, K7L 3N6 Canada

² National Research Council of Canada, Ottawa, Ontario, K1A 0A6 Canada

³ Department of Physics and Astronomy, Trent University, Peterborough, Ontario, K9J 7B8 Canada

Received 29 August 2012, revised 4 October 2012, accepted 1 November 2012

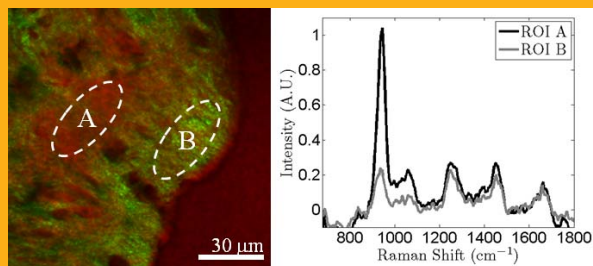
Published online 18 December 2012

Key words: Scanning microscopy, nonlinear microscopy, coherent anti-Stokes Raman scattering, biomaterials, cellulose, mineralogy



Supporting information for this article is available free of charge under <http://dx.doi.org/10.1002/jbio.201200171>

A simple scheme for multimodal coherent anti-Stokes Raman scattering (CARS) microscopy is based on the spectral focusing of ultrafast-oscillator-derived pump/probe light and synchronous photonic crystal fiber (PCF) fiber-generated broadband Stokes light. To date, such schemes allowed rapid hyperspectral imaging throughout the CH/OH high frequency region (2700–4000 cm^{-1}). Here we extend this approach to the middle (1640–3300 cm^{-1}) and fingerprint regions (850–1800 cm^{-1}) of the Raman spectrum. Our simple integrated approach to rapid hyperspectral CARS microscopy in the fingerprint region is demonstrated by applications to label-free multimodal imaging of cellulose and bulk bone, including use of the phosphate resonance at 960 cm^{-1} .



Label-free hyperspectral multimodal imaging of bulk bone. SHG (green) shows organization of collagen and CARS (red) contrast is obtained at the phosphate stretch, 960 cm^{-1} . Regions of varying phosphate density are confirmed by spectra.

1. Introduction

Coherent anti-Stokes Raman scattering (CARS) microscopy allows for label-free imaging of a wide range of molecular assemblies based on the resonant vibrational spectra of their constituents [1, 2]. Because of the stimulated nature of this nonlinear optical (NLO) process, CARS often yields signals that are orders of magnitude stronger than those ob-

tained using conventional Raman scattering. This allows for dramatically faster signal acquisition, a property that has transformed CARS from a strictly spectroscopic method to a burgeoning microscopy [1, 2]. Despite the utility of CARS for both microspectroscopy and rapid 3D imaging, often a given implementation trades off one capability for another. Emphasis is often placed on one of the following: 1) rapid imaging at fixed Raman shift, 2) recording a

* Corresponding author: e-mail: albert.stolow@nrc-cnrc.gc.ca, Phone: 613-993-7388, Fax: 613 991-3437

** These authors contributed equally to this work.

broad Raman spectrum, or 3), combining CARS with other techniques to achieve multimodal imaging [1, 3–9]. Spectral-focusing-based CARS microscopy (SF-CARS) [10–16] is a particularly simple and flexible implementation that permits balancing of these different features. It allows for both rapid contrast-based imaging and for the rapid scanning of the Raman shift, allowing facile recording of the Raman spectrum over the entire image. Such “hyperspectral imaging” has been used to study live cells and tissues [10–16] and has yielded spectra comparable to those obtained using multiplex CARS where emphasis is placed on acquiring broad, detailed CARS spectra at a few points, rather than on rapid imaging. Furthermore, because SF-CARS relies on standard femtosecond lasers and, in our implementation [12], photonic crystal fiber (PCF) sources, it allows for straightforward integration with existing nonlinear microscopes, and provides additional multimodal imaging options including second harmonic generation (SHG) and two-photon excitation fluorescence (TPEF) [12–14].

CARS is a vibrationally-resonant four-wave-mixing process that requires the input of (at least) two coherent laser pulses with frequency difference equal to that of the Raman mode under study [1, 2]. In SF-CARS microscopy, the first of these two beams (the pump/probe) is typically generated by a Ti:Sapphire oscillator. The need for a second beam – the Stokes – often requires additional elements such as an optical parametric oscillator or a second (synchronized) laser oscillator [10, 11]. Alternatively, SF-CARS can be implemented with a single ultrafast laser source, obtaining the Stokes pulse from either intra-pulse filtering (for ultrabroadband ~ 10 fs oscillators) [13, 15, 16], or from supercontinuum generation (SCG) in a commercial PCF module [12, 14, 16]. Such single-laser approaches feature simplicity of design, fast spectral scanning capability and low cost. However, SF-CARS has yet to demonstrate facile spectral scanning of both the fingerprint ($500\text{--}1800\text{ cm}^{-1}$) and the CH/OH regions ($2700\text{--}4000\text{ cm}^{-1}$) using a single setup. We note that some multiplex CARS implementations can record a wide CARS spectrum, however, image acquisition rates tend to be much lower [4–6].

Hyperspectral imaging in the congested fingerprint region is key to the expanded use of CARS microscopy in the biomedical and biomaterials imaging communities [17, 18]. To date, implementations of SF-CARS in both spectral regions have relied on a dual setup that alternately utilizes intra-pulse filtering or SCG [16]. Ideally, a single source of Stokes light should be used to scan the full Raman spectrum (intra-pulse filtering is unlikely, as this would require a high-power sub-2-fs laser source). There exist PCF-based SCG sources well-suited to imaging in the high frequency region [12, 19–22], but these have not been utilized for fingerprint region SF-

CARS, although new fibers may extend the effective spectral range [23]. Here we describe the extension of a simple multimodal SF-CARS technique to the fingerprint ($850\text{--}1800\text{ cm}^{-1}$) region. We demonstrate the utility of this approach with examples of hyperspectral multimodal imaging, here in bulk bone and cellulose biomaterials.

2. Experimental

For hyperspectral imaging in the fingerprint region, we modified an established multimodal CARS microscopy system based on a single Ti:Sapphire source and PCF-SCG, as described elsewhere [12]. A diagram of the setup is shown in Figure 1. Briefly, 60 fs pulses at a repetition rate of 80 MHz were generated by a Ti:Sapphire oscillator (Mira900, Coherent) and compressed by a prism-pair so that they were transform limited at the entrance to the PCF. A portion of this pump/probe beam was then directed to a PCF module (FemtoWhite-CARS, NKT Photonics) for SCG. The output of the PCF (Stokes) was filtered to remove <950 nm light, and recombined with the remaining pump/probe light which passed through a variable delay line. Two fixed blocks of high-dispersion SF-6 glass were used to match the linear chirp rates of the Stokes and pump/probe beams, with a 5-cm-long block inserted in the Stokes arm between the PCF and beam combiner and a 10-cm-long block inserted in the combined arm. By matching the chirp rates of these overlapping pulses, one controls their interaction bandwidth, allowing optimization of both spectral resolution and signal efficiency in the CARS process. This is known as spectral focusing [10–12]. Furthermore, by simply scanning the delay time between the pump and Stokes pulses, the CARS resonant frequency may be easily and rapidly tuned without adjusting any other components or requiring any realignment of the setup. This allows subsequent images to be taken at different effective Raman shifts. An example calibration curve is shown in Figure 1b, wherein absolute delay stage positions are correlated to the probed Raman shift. The Stokes is much broader spectrally and temporally than the pump and the calibration curve is largely a measure of the relative temporal distribution of the different spectral components of the Stokes. The calibration is linear in stage position, thus indicating that (at the very least) the Stokes is predominantly linearly chirped, even taking into account the higher order dispersion from of glass blocks.

If the entire CARS spectrum of a specific field of view (FOV) is of interest for hyperspectral imaging, many subsequent images can be acquired, allowing a CARS spectrum to be retrieved from the time stack of images for any pixel in the FOV. In practice, the

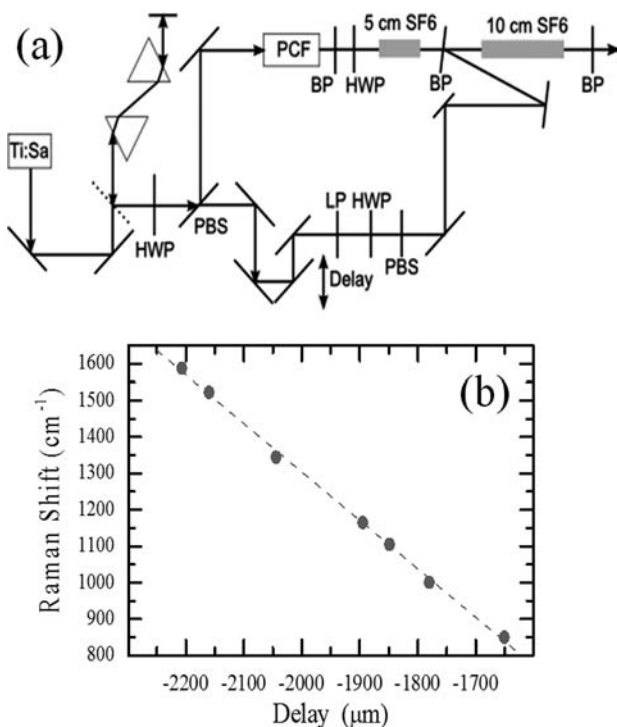


Figure 1 (a) Hyperspectral SF-CARS optical layout. Pulses from the Ti:Sa oscillator are sent through a prism compressor to ensure transform-limited behavior at the PCF. A variable beam splitter composed of a half-wave plate (HWP) followed by a polarizing beam splitter (PBS) was used to divide the beam. One arm was sent through a PCF, bandpass filter (BP), then a HWP before being sent through a 5 cm block of SF6. The other arm was sent through a longpass filter (LP) and a variable attenuator. The pump and Stokes were recombined on a second bandpass filter (BP). The angle of the BP in the diagram has been increased relative to the experimental conditions for clarity. After recombination, both beams were sent through a 10-cm block of SF6 glass. Depending on the wavelength used and the Raman mode probed, additional bandpass filters were inserted before the microscope. (b) CARS frequency calibration curve for spectral scans. The effective Raman shift between the pump and Stokes as a function of stage position can be measured at the microscope focus using four-wave mixing (i.e. nonresonant CARS signal) and/or sum frequency generation (in KDP powder, for example) signals collected with a spectrometer allowing the center wavelength of the signal to be measured. Despite passing broadband pulses through a fixed amount of high-dispersion glass, the resulting chirps are linear. Measured data points and their linear fit ($R^2 = 0.9985$) are shown.

speed of this process is limited by the pixel dwell-time and not by the scan speed of the delay stage. Spectral scanning also allows for the spectral resolution to be easily measured by scanning a known narrow linewidth feature and then deconvolving the instrument spectral response from the recorded

spectral width. For the data presented here, the spectral resolution was $27 \text{ cm}^{-1} \pm 2 \text{ cm}^{-1}$ and was measured by recording the CARS spectrum of the C–C bond in diamond at 1335 cm^{-1} ($\sim 2 \text{ cm}^{-1}$ FWHM) which can be easily deconvolved to allow an accurate measurement of the spectral resolution. While this spectral resolution is not ideal for all Raman modes studied in the fingerprint region, it represents a compromise between resolution and signal strength that has been found effective when working in the CH region [12]. As in previous work, the spectral resolution is presently but not fundamentally limited by the availability and selection of high dispersion glass blocks.

A FV300 Fluoview Olympus microscope was modified to allow for non-descanned CARS and SHG signal collection in the forward-direction via a multimodal optical fiber coupled to separate off-board PMT detectors, as described elsewhere [24]. The TPEF signal was simultaneously recorded via on-board descanned epi-detection. For most CARS experiments utilizing this setup, 15–22 mW of $>950 \text{ nm}$ broadband Stokes light and 80–200 mW of pump/probe light were measured at the entrance port of the microscope. Typically, a $40 \times 1.15 \text{ NA}$ water-immersion lens with cover-slip correction was used for multimodal imaging (Olympus UAPON 40XW340). The pixel dwell times used for acquisition ranged from $6.3 \mu\text{s}$ to $8.3 \mu\text{s}$, depending on the application. For some images, a live average was used, increasing the effective pixel dwell time. Without averaging, a single 256×256 frame could be acquired in 0.45–0.58 s, which is also the time step between images during hyperspectral imaging. As an example, in data presented here, images spanning a 1000 cm^{-1} spectral window were recorded with 1.6 cm^{-1} spectral steps between images. The total acquisition time for the full hyperspectral 3D data set was 280 seconds. In comparison with multiplex CARS microscopy where the entire CARS spectrum is acquired at a single pixel with pixel dwell times of several milliseconds, the hyperspectral data presented here had an effective pixel dwell time of 4.3 ms: Importantly, this is easily reduced by simply increasing the spectral scan step size between images. It is worth noting that the present hyperspectral CARS implementation is considerably faster than was demonstrated using commercial, temperature tuned OPOs [25].

We used a PCF with two zero-dispersion-points (ZDPs). This feature alters the spectral characteristics of the supercontinuum compared to more standard single-ZDP fibers used for multiplex CARS imaging [26–28]. The generated light has two separated continua, with two broad peaks residing on either side of the anomalous dispersion regime between the two ZDPs. The near-IR portion of the output of such a fiber is a spectrally-narrower conti-

num than is generated using a typical single ZDP fiber. This means that it contains relatively more spectral intensity at the relevant Stokes wavelengths, more efficiently generating the CARS signal. We used the FemtoWhite-CARS (NKT Photonics), which is a packaged SCG fiber module having ZDPs at 775 nm and 945 nm. The output of the PCF was shown to be relatively insensitive to an input wavelength between 775–945 nm, if the pulse duration and average power were kept constant [19, 22]. Thus, by simply tuning the centre wavelength of the Ti:Sapphire oscillator, the accessible CARS spectral window can be changed. Under typical conditions, 150–200 mW of post-compressor transform-limited pulses was split off for SCG: the emerging low-energy Stokes continuum extended from ~960 nm to 1200 nm, with a prominent peak at 1030–1050 nm, as shown in Figure 2a. As previously described [12], Stokes generation with 800 nm light allows efficient access to the CH/OH vibrational region; the energy difference between the pump/probe and Stokes

spans the 2400–4100 cm^{-1} region, with intensity maximum near 2880 cm^{-1} .

By tuning the Ti:Sapphire laser to longer wavelengths, the pump wavelength can be brought closer to that of the Stokes supercontinuum, and the CARS spectral window can therefore be shifted to lower frequencies into the fingerprint region. Four spectral windows are shown in Figure 2a–d. It is important to note that within a given spectral window, the CARS spectrum was routinely and rapidly recorded via time delay scans, as described above, requiring no active realignment or laser frequency tuning. To switch between spectral windows in hyperspectral CARS imaging, the Ti:Sapphire center wavelength must be changed along with the filters in the detection arm. The amount of dispersive glass can be changed, if needed.

For example, as shown in Figure 2b, generating a supercontinuum with 850 nm pump allowed for efficient access to Raman shifts of 1650–3300 cm^{-1} , spanning the “silent” spectral region, yet including

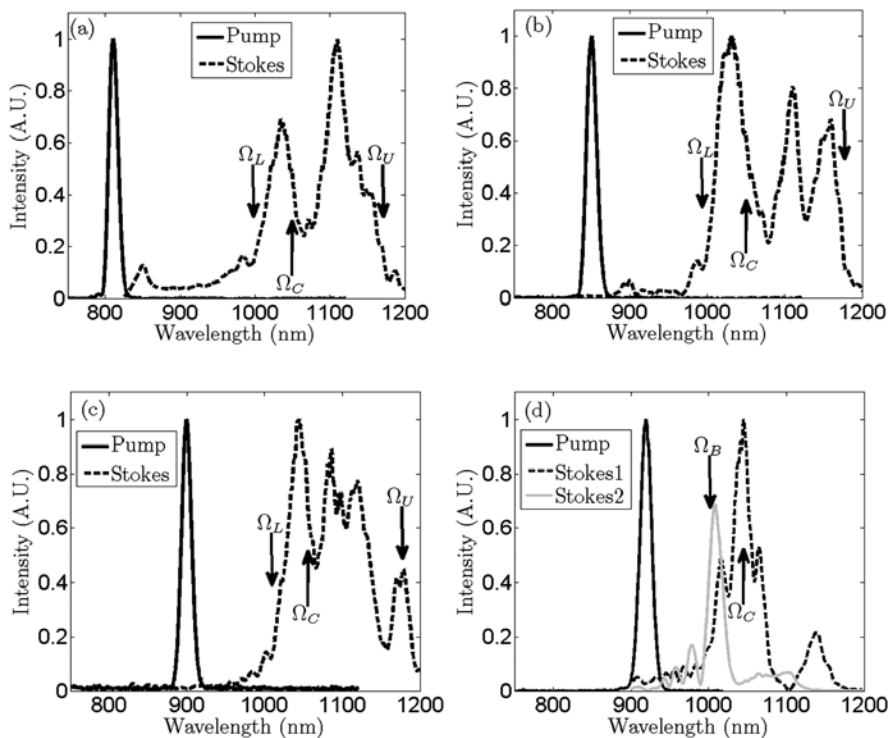


Figure 2 Stokes generation and CARS spectral regions accessible with the PCF module as a function of pump central wavelength and power. (a) With 150 mW of 805 nm pump, the Stokes continuum covers the CH– and OH– vibrational regions. Ω_L , Ω_C , and Ω_U correspond to approximate CARS frequencies 2400 cm^{-1} , 2900 cm^{-1} , and 3800 cm^{-1} , respectively. (b) With 150 mW of 850 nm pump, the Stokes continuum allows access across the $\Omega_L = 1650 \text{ cm}^{-1}$ to $\Omega_U = 3300 \text{ cm}^{-1}$, with considerable intensity in the $\Omega_C = 2240 \text{ cm}^{-1}$ ($\text{C}\equiv\text{N}$ stretch) frequency. (c) With 150 mW of 900 nm pump, the Stokes continuum allows access a large portion of the fingerprint region. Ω_L , Ω_C , and Ω_U correspond to approximate CARS frequencies 1150 cm^{-1} , 1550 cm^{-1} , and 2550 cm^{-1} , respectively. (d) With a nominal pump wavelength at 915 nm, using 150 mW of SCG power yields a Stokes spectrum that covers most of the fingerprint region, with a main peak around to $\Omega_C = 1300 \text{ cm}^{-1}$ (Stokes 1). Lowering the pump power to 40 mW generates a narrower Stokes continuum (Stokes 2) with efficient access to the phosphate resonance around $\Omega_B = 960 \text{ cm}^{-1}$. For comparison, the peak power densities of the 150 mW and 40 mW generated supercontinua are estimated to be 76 $\mu\text{W}/\text{nm}$ and 55 $\mu\text{W}/\text{nm}$, respectively.

both the CH-stretch resonance and the higher energy part of the fingerprint region. Likewise, most of the fingerprint region was accessed by tuning the Ti:Sapphire to 900 nm or beyond, where, as shown in Figure 2c, d, we accessed, for example, the 1100–2700 cm^{-1} region.

While part of the fingerprint region was easily accessed in this manner, it was challenging to reach lower CARS frequencies such as the phosphate ($\nu_1 \approx 960 \text{ cm}^{-1}$) or carbonate ($\nu_1 \approx 1075 \text{ cm}^{-1}$) resonances in bone. This is largely due to detection issues: under typical conditions for imaging the CH-stretch at 2880 cm^{-1} , the pump wavelength would be at 800 nm, with the anti-Stokes signal at 650 nm. However, as the pump laser is tuned to longer wavelengths, accessing smaller Raman shifts, the generated anti-Stokes signal likewise appears at longer wavelengths. At a pump wavelength of 900 nm, the anti-Stokes wavelength corresponding to a CARS resonance at 1100 cm^{-1} is at 818 nm, near the limit of detection for a typical red-sensitivity-enhanced PMT (e.g. Hamamatsu R3896). In our arrangement, there was sufficient spectral intensity in the Stokes pulse at 1015 nm to allow for imaging via the phosphate resonance at 960 cm^{-1} by using a pump wavelength of 925 nm. However, in this case the generated anti-Stokes signal was at 850 nm, where the red-enhanced PMT has 2.8% of the radiant sensitivity that it has at 650 nm.

To access the sub-1000 cm^{-1} region, we take advantage of the fact that the spectrum generated by the SCG module both narrows and experiences less red-shifting as the pump intensity is decreased. Because the generated signal in SF-CARS is typically limited by the available spectral intensity in the Stokes beam, one typically pumps the PCF with as much power as possible, limited by damage to the PCF. However, by lowering the pump intensity used for SCG, it is possible to bring the Stokes spectrum closer in frequency to that of the pump while maintaining a similar spectral intensity at the target wavelengths. Specifically, we found that by pumping the FemtoWhite-CARS module with as little as 40 mW of 915 nm light (rather than the typical 150–200 mW), we shift the Stokes spectrum below 1010 nm. While the resulting Stokes spectrum, shown in Figure 2d, is considerably narrower than typically used in our CARS experiments, it had nonetheless sufficient power and spectral bandwidth to span most of the fingerprint region – from 850–1850 cm^{-1} . This is demonstrated by a simple spectral scan of neat nitrobenzene, shown in Figure 3. A pump wavelength of 915 nm and a Stokes wavelength of 1000 nm generated the collected anti-Stokes signal at 840 nm. This wavelength is near the detection limit of our PMT which retains a sensitivity approximately 3 times greater than at 850 nm. In this case, 8 mW of Stokes power reached the microscope scan head. Thus, sim-

ply by tuning the Ti:Sapphire laser to longer wavelengths and significantly lowering the power for Stokes generation, we extended hyperspectral SF-CARS microscopy down to 850 cm^{-1} Raman shifts using our simple oscillator-PCF combination.

The coherent addition of vibrationally-resonant and (electronically) nonresonant CARS signals leads to significant differences between CARS and spontaneous Raman spectra [1, 2], thus complicating their direct comparison. The disparity between CARS and Raman spectra becomes glaring as the spectral density of resonances increases, and thus becomes acutely manifested in the fingerprint region. Stimulated Raman Scattering (SRS) is an alternative to CARS microscopy which is spectrally insensitive to the non-resonant background and which has recently been used for PCF-based spectral focusing in the fingerprint region [29]. However, for rapid imaging, SRS requires exceptionally low source noise, as well as additional optics and electronics [30]. An alternative approach is to use fast retrieval algorithms which convert CARS spectra to truer representations of spontaneous Raman spectra. These have been shown effective for retrieving Raman-like spectra from experimental CARS spectra in the fingerprint region [5, 6].

For the data presented here, we used a nonlinear Hilbert transform algorithm modified from that of Ref. [6]. This approach requires that the non-resonant background (NRB) spectrum associated with the CARS signal be accurately measured. To retrieve the most faithful spectrum, it is important to

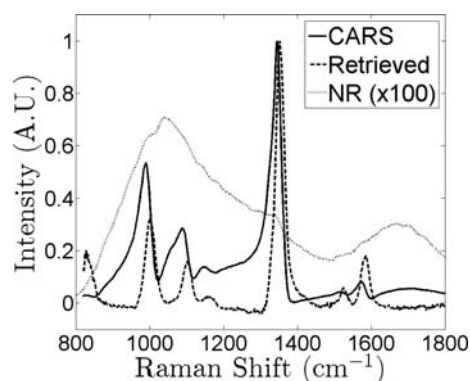


Figure 3 CARS spectrum from neat nitrobenzene obtained using SCG condition “Stokes 2” displayed in Figure 2d. Despite a relatively narrow Stokes continuum and low SCG output power, the entire fingerprint region from 850 cm^{-1} to 1800 cm^{-1} can be spanned at once. NR is the nonresonant background as simultaneously obtained from glass and used in the Hilbert transform retrieval algorithm that converts the CARS spectrum to a retrieved spectrum which closely resembles that measured via spontaneous Raman spectroscopy (see supplemental information). These spectra were retrieved from an image of glass in nitrobenzene, recorded with a pixel dwell time of $6.3 \mu\text{s}$ then smoothed (three frames running average).

obtain the NRB spectrum simultaneously with the CARS image. This is particularly simple using the setup presented here because the CARS spectrum was typically recorded at every pixel in the FOV. Thus, we acquired the NRB by measuring the spectral response in a region of interest (ROI) within our FOV that was relatively free of resonant material and used an average spectrum over this ROI for input into the retrieval algorithm. This simultaneous acquisition of NRB and CARS had the advantage of compensating for any medium-to-long-term drifts in the system. For comparison, in Figure 3 we show characteristic CARS and NRB spectra together with the retrieved Raman-like spectrum of pure nitrobenzene. In the supplementary material, we compare this retrieved Raman spectrum with a spontaneous Raman spectrum. It should be noted that the absolute magnitude of the NRB is not relevant for the retrieval algorithm; only the form of the spectral response is needed [6]. Thus, the retrieval algorithm works even in the presence of a relatively strong NRB as long as it is measured in the same FOV.

In the following, we demonstrate the utility of this approach to hyperspectral multimodal CARS imaging in the fingerprint region via studies of cellulose and bovine rib bones. Cellulose was taken from lab-grade cotton swabs (Puritan Medical) and hydrated in tap water on a microscope slide and covered with a coverslip. Bone samples were sliced with a scalpel or cut into thin wedges with a diamond saw, rinsed with ethanol for sterilization, and hydrated on a microscope well-slide with coverslip.

3. Results and discussion

Cellulose is a biologically inert carbohydrate polymer that is important for many industrial sectors and is used in artificial tissue engineering [31, 32]. Natural and synthetic (or processed) cellulosic fibers organize into aligned crystalline manifolds with varying degrees of organization and crystallinity leading to varying material properties. Traditionally, X-ray crystallography and Raman spectroscopy have been used for characterizing cellulose crystallinity and structure [33–35]. In particular, polarization-resolved vibrational spectroscopy has proven to be a powerful tool for discerning bond orientation directions in cellulose [35–39]. However, due to relatively low signal levels, Raman micro-spectroscopy is still largely a spectroscopic technique and remains challenging for use in a full-fledged 3D microscopic imaging capacity. The application of nonlinear microscopy to cellulose research is largely confined to the use of second harmonic generation, as the quasi-crystalline fibers generate strong polarization-dependant signals [40–42]. The

utility of SHG as an imaging modality for cellulose, combined with the need for rapid chemically-selective imaging motivated the combination of CARS and SHG for the imaging of cellulose and other structured carbohydrate biopolymers, where CARS was either used to show polarization-resolved bond orientation based on contrast at the CH– [14, 43] and OH– stretch resonances [14], or simply to provide general CH-stretch contrast for non-cellulose components such as cells [44]. From Raman studies, it is acknowledged that the best discrimination for orientation alignment exists in the fingerprint region [35, 39]. Furthermore, different native and artificial cellulose fibers demonstrate different polarization anisotropies in their Raman spectra in the fingerprint region, but show very little differences in the CH– and OH– spectral ranges [32]. We demonstrate here that polarization-resolved CARS spectra in the fingerprint are highly sensitive to bond-orientation in cotton cellulose fibers by acquiring hyperspectral images of cellulose and using the Hilbert transform to recover the Raman spectrum. An example raw hyperspectral image stack may be seen in the supplementary material (Media 1) where a movie shows the entire CARS spectral scan from ~ 1000 – 2000 cm^{-1} . These spectral scan results are summarized in Figure 4 where it can be seen that the retrieved CARS signals at 1130 cm^{-1} , 1340 cm^{-1} , and 1420 cm^{-1} are considerably stronger when all CARS fields are polarized along the fiber axis, compared to being polarized orthogonal to the fiber axis. Furthermore, a moderate peak at 1460 cm^{-1} shows reversal of this behavior, and is more intense when the polarization is orthogonal to the fiber axis. This is in excellent agreement with the known Raman spectral trends [35, 39], and highlights the utility of rapid label-free multimodal imaging for such biomaterial systems.

Ratiometric analysis of vibrational spectra is a useful indicator of internal stresses in cellulose fibers [37]. Fingerprint hyperspectral CARS imaging should find use in the non-destructive monitoring of cellulose biomaterial growth, where it can provide more rapid imaging than can Raman microscopy and simultaneously offers the additional modalities of SHG and TPEF imaging.

Cellulose scaffolds are of particular interest in bone genesis tissue engineering applications, where they act as functional substrates that promote the synthesis of collagen and subsequent mineralization of bone in osteocytes [45]. This process of osteogenesis and mineralization of hydroxyapatite, both in vivo and in vitro, is of considerable research interest, and the precise roles of collagen, lipids and cholesterol, and osteoblasts are actively under study [46–49]. Spontaneous Raman microspectroscopy has proven a valuable tool for chemical analysis of bone [50–52], but has rarely been utilized for detailed imaging due to relatively long pixel dwell-times and

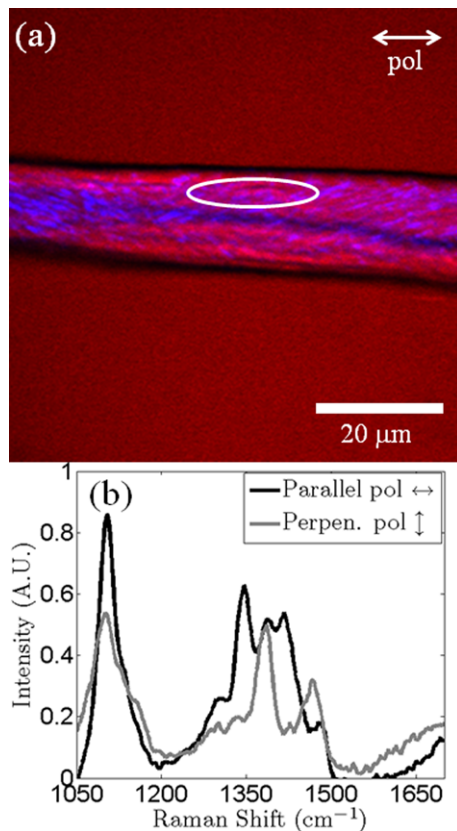


Figure 4 Polarization-dependent CARS + SHG imaging of cellulose (cotton) fibers in water. **(a)** Overlaid CARS image taken at 1090 cm^{-1} (red), and SHG (blue) taken simultaneously. Both images are an average of two frames (effective pixel dwell time $12.6\text{ }\mu\text{s}$). The CARS image is an unprocessed, false-colored frame from a hyperspectral stack (see the movie Media 1 in the supplemental material). Pump and Stokes beams were polarized along the fiber's long axis (horizontal). **(b)** CARS-retrieved-Raman spectrum averaged from the indicated ROI in **(a)**, obtained with polarizations both parallel (\leftrightarrow) and perpendicular (\downarrow) to the fiber axis. For each case, the CARS spectrum was acquired for the entire image in 280 s (626 frames, 0.45 s per frame, 1.6 cm^{-1} change in effective Raman shift per frame). Spectra were smoothed using a three frame running average.

poor spatial resolution [53]. The desire to follow the processes of osteogenesis and mineralization in a label-free manner has motivated the application of multimodal microscopy to bone imaging, where SHG is used to image collagen [45] (and/or cellulose [45, 52, 53]), endogenous TPEF visualizes calcified cartilage [53], and CARS monitors either general cellular architecture (via CH-stretch at 2800 cm^{-1} – 2950 cm^{-1}) [45, 53] or the phosphate signal from bone in the fingerprint region [49, 55, 56].

We illustrate the potential of our simple multimodal CARS technique for hyperspectral imaging of bone in the fingerprint region in Figure 5, where

CARS + TPEF + SHG microscopy is applied to bulk bovine rib bones. Here, SHG visualizes the collagen matrix swirling around an osteon, the centre of which provides endogenous TPEF from blood. The surrounding cortical bone is imaged with CARS, with contrast via the phosphate peak at 960 cm^{-1} . A hyperspectral image set is also recorded (533 frames, 0.89 s per frame, 800 – 1800 cm^{-1}) from which we recover the CARS-retrieved-Raman spectrum from the cortical bone tissue showing a well-resolved pair of peaks for phosphate (960 cm^{-1}) and carbonate (1075 cm^{-1}). Furthermore, other Raman peaks associated with bulk bone are visible, including the peaks associated with amide III ($\sim 1275\text{ cm}^{-1}$), C–H bending ($\sim 1425\text{ cm}^{-1}$), and amide I ($\sim 1650\text{ cm}^{-1}$) modes [50]. Besides applications to biomaterial research and live-cell imaging, this demonstration of label-free CARS microscopy of bulk bone promises to find clinical applications in bone cancer and osteoporosis diagnosis. However, such applications will require the demonstration of hyperspectral imaging in the backwards (epi-) direction. While epi-CARS signals are notoriously weaker than forward-CARS, the signal at 960 cm^{-1} was found to be sufficiently strong that, with a proper red-enhanced PMT or APD detector [56], we believe that backwards-detection should be feasible. Nonetheless, the use of this technique for monitoring osteogenesis (or even osteoporosis) would strongly benefit from an ability to quantify bone mineral density. In Figure 6 we show an image overlay of CARS (at 960 cm^{-1}) and SHG in bone where increased SHG from collagen is broadly anti-correlated with the CARS signal from phosphate, as seen from a quasi-quantitative spectral analysis. Again, hyperspectral imaging is performed (474 frames, 1.34 s per frame, 800 – 1800 cm^{-1}) to further characterize this apparent anti-correlation. Here, two nearby regions of interest are shown to yield the same (but independently retrieved) spectra for the organic matrix, but large differences in the relative amount of mineral material as indicated by the phosphate (960 cm^{-1}) and carbonate (1075 cm^{-1}) peaks. The change in mineral content is strongly anti-correlated with the SHG measured from the same ROI. This result shows the power of combining SHG with hyperspectral CARS imaging. This technique is sensitive to differences in phosphate concentration, and, with improved quantification, holds strong potential for microscopic measurements of bone density. A key aspect of our SF-CARS technique is that we can choose to operate either in a fixed-frequency-contrast rapid imaging modality, or can rapidly scan the Raman shift to obtain the CARS spectrum, as needed. The ability to monitor the CARS spectrum is an important feature for future quantitative work because “on-peak” signal contrast monitoring cannot distinguish between reduction of signal due to density fluctuations or due to slight spectral

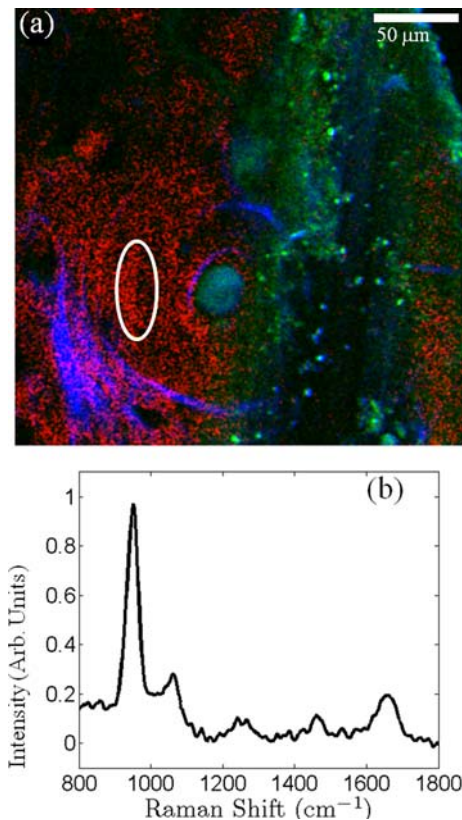


Figure 5 Label-free multimodal imaging of osteon in cortical bone. (a) Simultaneously obtained epi-TPEF (green) and SHG (blue), and forward-collected hyperspectral CARS imaging (red), with chemical contrast at the 960 cm^{-1} phosphate peak of hydroxyapatite. Endogenous TPEF from blood within the Haversian canal is surrounded by SHG from the collagen matrix. Sample thickness is $100\text{ }\mu\text{m}$. (b) A CARS-retrieved spectrum from the highlighted ROI in (a) reproduces the Raman spectrum from bulk bone [50], including sharp phosphate and carbonate peaks at the lower frequencies, and organic peaks between 1200 cm^{-1} – 1800 cm^{-1} . The 533-frame hyperspectral image stack was collected in 0.89 s per frame, and spans a CARS frequency range of 800 – 1800 cm^{-1} . The spectrum was smoothed using a three frame running average. For clarity, the three channel image has been separated into three grey-scale images which are included in the supplementary material.

shifts of the vibrational resonances. Such shifts in the phosphate peak are known to be a function of mineral deposition age and bone maturity [57].

4. Summary

Implementations of CARS microscopy based on spectral focusing can be easily integrated with other nonlinear optical imaging modalities such as SHG and TPEF, providing a simple yet powerful technolo-

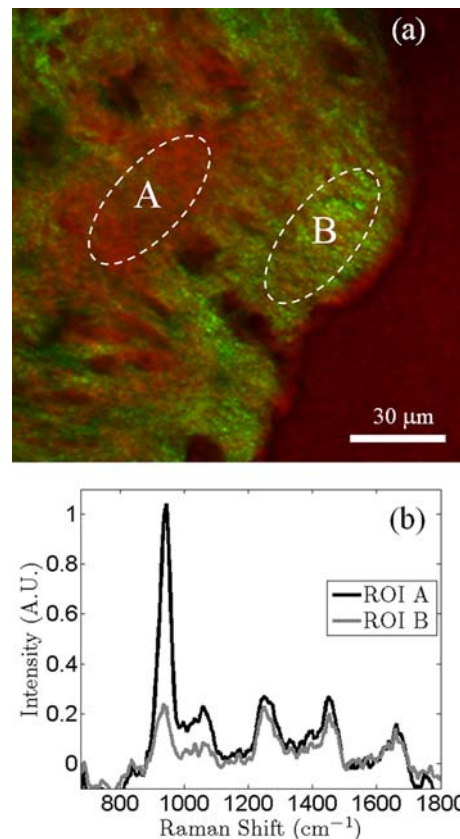


Figure 6 Bone density and collagen SHG. (a) Simultaneously obtained SHG (green) and hyperspectral CARS (red; contrast at 960 cm^{-1}) images of bovine rib bone. Within the field of view, regions of high collagen content (bright green, ROI B) and lower collagen content (ROI A) are identified. Sample thickness is $100\text{ }\mu\text{m}$. (b) CARS-retrieved-Raman spectra from ROI A and B demonstrate that in the regions of high SHG signal, a lower bone mineral density is found compared to regions with lower SHG signal. Spectra from ROI A and ROI B are retrieved independently but indicate almost identical amounts of organic material (see peak at 1625 cm^{-1}) yet drastically different amounts of hydroxyapatite (see peak at 960 cm^{-1}). The 475-frame hyperspectral image stack was collected in 1.34 s per frame, and spans a CARS frequency range of 800 – 1800 cm^{-1} . Spectra were smoothed using a three frame running average.

gical solution to label-free hyperspectral imaging needs. In this article, we described how a particular implementation based on a single femtosecond oscillator source, with subsequent Stokes generation in a PCF, can be extended continuously from the CH/OH vibrational frequency range to the fingerprint region. Specifically, we show that reducing the pump power for PCF-based Stokes generation allows for imaging down at 850 cm^{-1} , using a standard red-enhanced PMT. As a demonstration of the utility and capabilities of this simple approach, we presented the hyper-

spectral multimodal CARS imaging of biomaterials such as cellulose fibers and biological samples such as bulk bone. We find that the combination of polarization-controlled CARS in the fingerprint region with SHG imaging provides straightforward indications of bond orientations in cellulose. We furthermore demonstrated the utility of this technique to monitor bone mineral density in relatively thick tissue samples, motivating the application of this method to live-cell imaging in future osteogenesis experiments.

Acknowledgements The authors would like to thank Robert C. Burruss of the USGS, Marcus Cicerone of NIST, Daniel Côté of Université Laval, and Rune Lausten (NRC) for fruitful discussions. We thank Chris Kingston of the NRC for obtaining the Raman spectrum of nitrobenzene. This research was funded by a NRC-NSC-ITRI Canada-Taiwan Cooperation project “Digital FLIM-CARS Microscopy” and by a NSERC Discovery grant (AS).

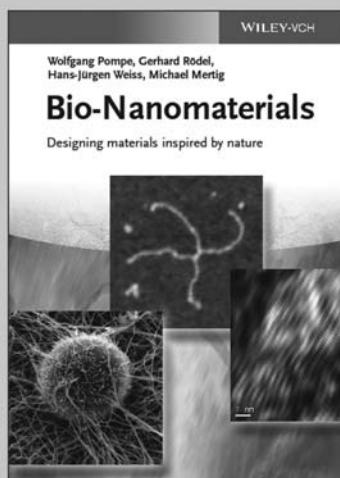
Author biographies Please see Supporting Information online.

References

- [1] C. L. Evans and X. S. Xie, *Annu. Rev. Anal. Chem.* **1**, 883–909 (2008).
- [2] T. T. Le, S. Yue, and J.-X. Cheng, *J. Lipid Res.* **51**, 3091–3102 (2010).
- [3] J. X. Cheng, A. Volkmer, L. D. Book, and X. S. Xie, *J. Phys. Chem. B* **106**, 8493–8498 (2002).
- [4] M. Muller and J. M. Schins, *J. Phys. Chem. B* **106**, 3715–3723 (2002).
- [5] H. A. Rini, M. Bonn, M. Muller, and E. M. Vartiainen, *ChemPhysChem* **8**, 279–287 (2007).
- [6] Y. Liu, Y. J. Lee, and M. T. Cicerone, *Opt. Lett.* **34**, 1363–1365 (2009).
- [7] X. Nan, A. M. Tonary, A. Stolow, X. S. Xie, and J. P. Pezacki, *ChemBioChem* **7**, 1895–1897 (2006).
- [8] A. Downes, R. Mouras, and A. Elfick, *J. Raman Spectrosc.* **40**, 757 (2009).
- [9] T. T. Le, I. M. Langohr, M. J. Locker, M. Sturek, and J.-X. Cheng, *J. Biomed. Opt.* **12**, 054007 (2007).
- [10] T. Hellerer, A. M. Enejder, and A. Zumbusch, *Appl. Phys. Lett.* **85**, 25–27 (2004).
- [11] I. Rocha-Mendoza, W. Langbein, and P. Borri, *Appl. Phys. Lett.* **93**, 201103 (2008).
- [12] A. F. Pegoraro, A. Ridsdale, D. J. Moffatt, Y. Jia, J. P. Pezacki, and A. Stolow, *Opt. Express* **17**, 2984–2996 (2009).
- [13] W. Langbein, I. Rocha-Mendoza, and P. Borri, *Appl. Phys. Lett.* **95**, 081109 (2009).
- [14] A. D. Slepko, A. Ridsdale, A. F. Pegoraro, D. J. Moffatt, and A. Stolow, *Biomed. Opt. Express* **1**, 1347–1357 (2010).
- [15] B.-C. Chen, J. Sung, and S.-H. Lim, *J. Phys. Chem. B* **114**, 16871–16880 (2010).
- [16] B.-C. Chen, J. Sung, Xiaoxi Wu, and S.-H. Lim, *J. Biomed. Opt.* **16**, 021112 (2011).
- [17] Y. Zeng, B. Saar, M. Friedrich, F. Chen, Y.-S. Liu, R. Dixon, M. Himmel, X. Xie, and S.-Y. Ding, *Bio-Energy Research* **3**, 272–277 (2010).
- [18] C. Brackmann, A. Bengtsson, M. L. Alminger, U. Svanberg, and A. Enejder, *J. Raman Spectrosc.* **42**, 586–592 (2011).
- [19] K. M. Hilligsøe, T. Andersen, H. Paulsen, C. Nielsen, K. Mølmer, S. Keiding, R. Kristiansen, K. Hansen, and J. Larsen, *Opt. Express* **12**, 1045–1054 (2004).
- [20] E. R. Andresen, H. N. Paulsen, V. Birkedal, J. Thøgersen, and S. R. Keiding, *J. Opt. Soc. Am. B* **22**, 1934–1938 (2005).
- [21] E. R. Andresen, V. Birkedal, J. Thøgersen, and S. R. Keiding, *Opt. Lett.* **31**, 1328–1330 (2006).
- [22] S. Murugkar, C. Brideau, A. Ridsdale, M. Naji, P. K. Stys, and H. Anis, *Opt. Express* **15**, 14028–14037 (2007).
- [23] P. Klarskov, A. Isomaki, K. P. Hansen, and P. E. Andersen, *Opt. Express* **19**, 26672–26683 (2011).
- [24] A. D. Slepko, A. Ridsdale, H.-N. Wan, M.-H. Wang, A. F. Pegoraro, D. J. Moffatt, J. P. Pezacki, F.-J. Kao, and A. Stolow, *J. Biomed. Opt.* **16**, 021103 (2011).
- [25] R. S. Lim, J. L. Suhaimi, S. Miyazaki-Anzai, M. Miyazaki, M. Levi, E. O. Potma, and B. J. Tromberg, *J. Lipid Res.* **52**, 2177 (2011).
- [26] T. W. Kee and M. T. Cicerone, *Opt. Lett.* **29**, 2701–2703 (2004).
- [27] H. Kano and H. O. Hamaguchi, *Opt. Express* **13**, 1322–1327 (2005).
- [28] B. von Vacano, W. Wohlleben, and M. Motzkus, *Opt. Lett.* **31**, 413–415 (2006).
- [29] E. R. Andresen, P. Berto, and H. Rigneault, *Opt. Lett.* **36**, 2387–2389 (2011).
- [30] W. Min, C. W. Freudiger, S. Lu, and X. S. Xie, *Annu Rev Phys Chem* **62**, 507–530 (2011).
- [31] S. J. Eichhorn, C. A. Baillie, N. Zafeiropoulos, L. Y. Mwaikambo, M. P. Ansell, A. Dufresne, K. M. Entwistle, P. J. Herrera-Franco, G. C. Escamilla, L. H. Groom, M. Hughes, C. Hill, T. G. Rials, and P. M. Wild, *J. Mater. Sci.* **36**, 2107–2131 (2001).
- [32] D. Klemm, B. Heublein, H.-P. Fink, and A. Bohn, *Angew. Chem. Int. Ed.* **44**, 3358–3393 (2005).
- [33] P. Zugenmaier, *Crystalline Cellulose and Cellulose Derivatives* (Springer, Berlin, 2008).
- [34] P. M. Fechner, S. Wartewig, P. Kleinebudde, and R. H. H. Nuebert, *Carbohydr. Res.* **340**, 2563–2568 (2005).
- [35] J. H. Wiley and R. H. Atalla, *Carbohydr. Res.* **160**, 113–129 (1987).
- [36] A. Šturcová, I. His, T. J. Wess, G. Cameron, and M. C. Jarvis, *Biomacromolecules* **4**, 1589–1595 (2003).
- [37] M. C. Jarvis and M. C. McCann, *Plant Physiol. Biochem.* **38**, 1–13 (2000).
- [38] B. Hinterstoisser, M. Akerholm, and L. Salmen, *Carbohydr. Res.* **334**, 27–37 (2001).
- [39] N. Gierlinger, S. Luss, C. König, J. Konnerth, M. Eder, and P. Fratzl, *J. Exp. Bot.* **61**, 587–595 (2010).

- [40] Y. Marubashi, T. Higashi, S. Hirakawa, S. Tani, T. Erata, M. Takai, and J. Kawamata, *Opt. Rev.* **11**, 385–387 (2004).
- [41] O. Nadiarnykh, R. B. LaComb, P. J. Campagnola, and W. A. Mohler, *Opt. Express* **15**, 3348–3360 (2007).
- [42] R. M. J. Brown, A. C. Millard, and P. J. Campagnola, *Opt. Lett.* **28**, 2207–2209 (2003).
- [43] M. Zimmerley, R. Younger, T. Valenton, D. C. Oertel, J. L. Ward, and E. O. Potma, *J. Phys. Chem. B* **114**, 10200–10208 (2010).
- [44] C. Brackmann, A. Bodin, M. Åkeson, P. Gatenholm, and A. Enejder, *Biomacromolecules* **11**, 542–548 (2010).
- [45] C. Brackmann, M. Zaborowska, J. Sundberg, P. Gatenholm, and A. Enejder, *Tissue Engineering Part C: Methods* **18**, 227–234 (2012).
- [46] L. C. Palmer, C. J. Newcomb, S. R. Kaltz, E. D. Spoerke, and S. I. Stupp, *Chem. Rev.* **108**, 4754–4783 (2008).
- [47] D. Laird, M. Mucalo, and Y. Yokogawa, *J. Colloid Interface Sci.* **295**, 348–363 (2006).
- [48] B. Boyan, Z. Schwartz, L. Swain, and A. Khare, *Anat. Rec.* **224**, 211–219 (1989).
- [49] Martin Jurna, *Vibrational Phase Contrast CARS Microscopy*, Ph.D. thesis, University of Twente (2010).
- [50] A. Carden and M. D. Morris, *J Biomed Opt.* **5**, 259–268 (2000).
- [51] S. Gamsjaeger, A. Masic, P. Roschger, M. Kazanci, J. W. C. Dunlop, K. Klaushofer, E. P. Paschalis, and P. Fratzl, *Bone* **47**, 392–399 (2010).
- [52] J. Burket, S. Gourion-Arsiquaud, L. M. Havill, S. P. Baker, A. L. Boskey, and M. C. H. van der Meulen, *J. Biomech.* **44**, 277–284 (2011).
- [53] J. A. Timlin, A. Carden, M. D. Morris, J. F. Bonadio, C. E. Hoffler, K. M. Kozloff, and S. A. Goldstein, *J. Biomed. Opt.* **4**, 28 (1999).
- [54] J. C. Mansfield and C. P. Winlove, *J. Anat.* **220**, 405–416 (2012).
- [55] S. H. Parekh, K. Chatterjee, S. Lin-Gibson, N. M. Moore, M. T. Cicerone, M. F. Young, and C. G. Simon Jr, *Biomaterials* **32**, 2256–2264 (2011).
- [56] A. Downes, R. Mouras, P. Bagnaninchi, and A. Elfick, *J. Raman Spectrosc.* **42**, 1864–1870 (2011).
- [57] R. Mendelsohn, E. P. Paschalis, P. J. Sherman, and A. L. Boskey, *Appl. Spectrosc.* **54**, 1183–1191 (2000).

+++ NEW +++ NEW +++ NEW +++ NEW +++ NEW +++ NEW +++ NEW +++



2013. 470 Pages, Hardcover
122 Fig. (2 Colored Fig.)
ISBN 978-3-527-41015-6

WOLFGANG POMPE / GERHARD RÖDEL / HANS-JÜRGEN WEISS /
MICHAEL MERTIG

Bio-Nanomaterials

Designing materials inspired by nature

Written by authors from different fields to reflect the interdisciplinary nature of the topic, this book guides the reader through new nanomaterials processing inspired by nature. Structured around general principles, each selection and explanation is motivated by particular biological case studies. This provides

the background for elucidating the particular principle in a second section. In the third part, examples for applying the principle to materials processing are given, while in a fourth subsection each chapter is supplemented by a selection of relevant experimental and theoretical techniques.

Register now for the free
WILEY-VCH Newsletter!
www.wiley-vch.de/home/pas

WILEY-VCH • P.O. Box 10 11 61 • 69451 Weinheim, Germany
Fax: +49 (0) 62 01 - 60 61 84
e-mail: service@wiley-vch.de • <http://www.wiley-vch.de>

WILEY-VCH